Incipient ferroelectricity: A route towards bulk-terminated SrTiO₃

Igor Sokolović, Michael Schmid, Ulrike Diebold, and Martin Setvin[*]

Institute of Applied Physics, TU Wien, Wiedner Hauptstrasse 8-10/134, 1040 Vienna, Austria

An investigation of bulk-terminated (001) surfaces of SrTiO₃, a prototypical cubic perovskite, was made possible with a novel cleaving procedure. Controlled application of strain on a SrTiO₃ single-crystal results in a flat cleavage with μm-size domains of SrO and TiO₂. Distribution of these two terminations is dictated by ferroelectric domains induced by strain during the cleavage process. Atomically resolved scanning tunneling microscopy/atomic force microscopy measurements reveal the presence of point defects in a well-defined concentration of $(14 \pm 2)\%$; Sr vacancies form at the SrO termination and complementary Sr adatoms appear at the TiO₂ termination. These intrinsic defects stabilize the surface by balancing the interplay between ferroelectricity, surface polarity, and surface charge.

Perovskite oxides attract increasing attention due to their broad potential in many applications [1–3]. Understanding their surfaces is challenging because the ternary composition of the bulk leads to multiple stable surface terminations. SrTiO₃ is the prototypical cubic perovskite oxide, interesting for its catalytic and photocatalytic properties [4], potential use in oxide electronics [5–8], and for fundamental phenomena including the appearance of two-dimensional electron gas at its surfaces [9–11] and interfaces [3]. The SrTiO₃(001) surface plays a key role in all these functionalities, but the available surface studies of this facet illustrate a general problem of approaching perovskite materials: A plethora of various surface terminations can form, depending on the preparation technique and on slight changes in the surface stoichiometry. The center of interest typically lies in bulk-terminated perovskite surfaces, because wet chemical preparation methods typically provide surfaces with a (1×1) diffraction pattern [7]. Yet this surface preparation method is problematic due to the possible presence of amorphous structures [12] or contaminants [13].

Despite the intensive and long-lasting scientific interest in this material, we are not aware of any work leading to atomic-scale characterization of the bulk-terminated SrTiO₃ surface. Cleaving a single crystal would be an obvious solution for obtaining a pristine surface [14–16], but the main impediment is that cubic perovskites typically do not possess a natural cleavage plane. Instead, they exhibit the so called conchoidal fracture (see Fig. S1 in the Supplemental Material [17]). An alternative technique for surface preparation is applying cycles of sputtering and high-temperature annealing, a standard procedure used for preparing oxide surfaces in ultrahigh vacuum (UHV). For perovskite surfaces, however, this method results in a series of complex reconstructions [18–20], which are very stable and chemically inert, exactly the opposite to the desired behavior of perovskites in most applications.

Here AFM/STM measurements were performed in an UHV chamber with a base pressure below 2×10^{-11} mbar, equipped with a ScientaOmicron LT STM/AFM at $T = 4.8$ K, using the qPlus setup with a separate wire [21] for the tunneling current and a differential cryogenic preamplifier [22]. Etched tungsten tips were glued on the tuning fork and cleaned by self-sputtering in Ar atmosphere [23] prior to the experiment. The resonance frequency of the qPlus cantilevers was 77 kHz with a Q factor of $\approx$50000. Scanning tunneling spectroscopy (STS) data were measured using the lock-in detection ($f = 123$ Hz, $A = 10$ mV), and a data processing method described in Ref. [24] was used to suppress noise around the Fermi level. SrTiO₃ samples (CrysTec) with 0.5 wt% Nb doping were used. Samples with polished (110) surfaces were cut into 1 mm thick 3.5×7 mm² rectangles. The cleavage was performed along the (001) plane, i.e., perpendicular to the polished surface. Surface profiles were measured on a Bruker DektakXTL profiler.

Our previous study on KTaO₃ [25] indicated that ferroelectricity induced in a perovskite can create a natural cleavage plane oriented perpendicular to the electric polarization. SrTiO₃ is an incipient ferroelectric material: Its ferroelectric Curie temperature lies below 0 K, but can even be shifted to above room temperature [26] when the c axis is sufficiently elongated to suppress the antiferroelectric lattice distortions [27–29]. This can be achieved by application of compressive or tensile strain in a direction perpendicular or parallel to the intended polarization direction, respectively.

Based on these considerations we have designed the device for cleaving SrTiO₃, sketched in Fig. 1(a). It is based on compressing the STO single crystal along the [110] direction from the side in two regions, while sparing a small fraction of the volume [shaded in Fig. 1(a)] where the cleavage is intended to occur. The cleaving is performed by pushing the crystal ($\mathbf{F}_{\text{ext}}$) along the [110] axis, which induces additional strain, strongly confined in the shaded region [see Fig. 1(b)]. In contrast to unstrained crystals, samples properly prestrained prior to the cleaving become brittle and readily cleave along the (001) plane. A successful cleavage is shown in Fig. 1(c).
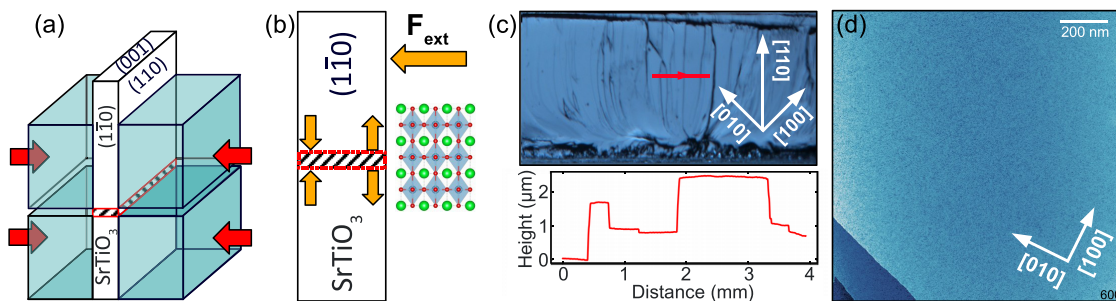
———
*setvin@iap.tuwien.ac.at

FIG. 1. Cleaving SrTiO₃. (a) Drawing of the sample mount. A SrTiO₃ sample is pressed by steel blocks to induce directed strain in the cleavage region. (b) Sketch of the strain distribution during the cleavage process (orange) and the unit cell distortion (Sr - green, Ti - blue, O - red; the distortion is not to scale). (c) Photograph of the as-cleaved surface. A height profile measured along the red arrow shows that all facets are flat and have the same (001) orientation. (d) Large-area STM image ($I_T = 2$ pA, $V_s = +3.3$ V, 1.5×1.5 μm²) of the as-cleaved surface, showing μm-sized flat regions and steps with a height of one unit cell.

The surface is characterized by a train of terraces separated by macroscopic steps oriented along the [110] direction (parallel to the external strain). A large-area STM image of a SrTiO₃ (001) surface cleaved by this method is displayed in Fig. 1(d). The surface consists of atomically flat terraces ranging from ≈50 nm up to several μm in size (see Fig. S2 [17] for more examples).

Using combined STM/AFM, we have identified two distinct terminations. Figures 2 and 3 show areas terminated with top layers of SrO and TiO₂, respectively. Figure 2(a) shows a constant-height STM image; the area marked by the dashed square is imaged by AFM in Fig. 2(b). A clear, bulk-terminated (1 × 1) pattern is observed in AFM, while the STM image only shows electronic contrast. The lack of atomic resolution in STM is attributed to an absence of

localized surface states associated with the atoms' positions. Superimposed on Fig. 2(b) is a ball model of the (1 × 1) SrO surface structure. This termination is not perfect as there are point defects in the form of missing atoms. We observe only one single type of vacancies, which, in principle, could be either missing O or Sr atoms. The defect type cannot be determined solely from AFM images, since the contrast achieved on ionic crystals is tip dependent: Cation-terminated tips interact attractively with surface anions and repulsively with cations [30,31], while an anion-terminated tip will show an inverted contrast (see Fig. S3). The unit-cell grid superimposed on the atomically resolved AFM image of the SrO termination [Fig. 2(d)] reveals that all the vacancies appear in equivalent lattice positions, with a concentration of
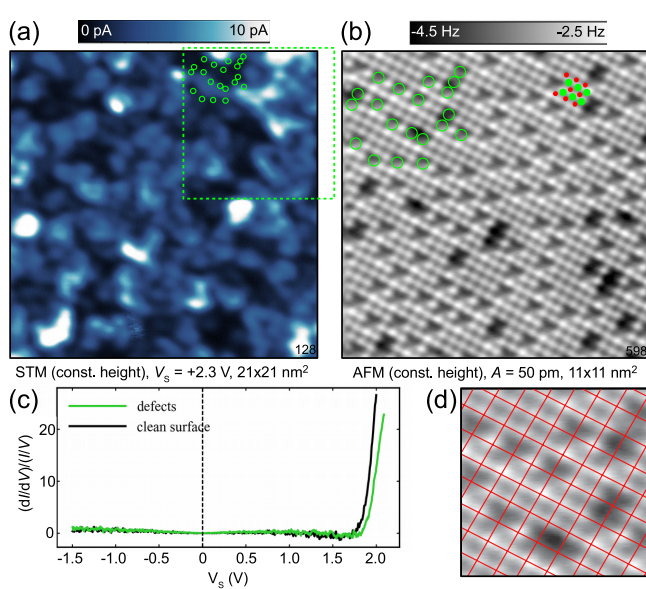

FIG. 2. SrO termination. (a) STM image and (b) AFM image of the square marked in (a) with the Sr/O atoms sketched in green/red, and point defects highlighted by the open green circles. (c) STS spectra measured above the clean surface and above the point defects. (d) Unit-cell grid superimposed on the atomically resolved AFM image.
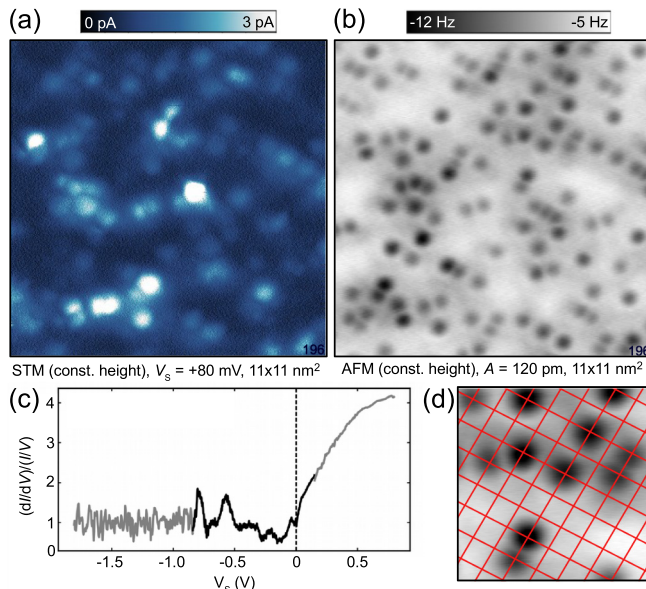

FIG. 3. TiO₂ termination. (a) STM image and (b) AFM image of the same area measured simultaneously. (c) STS spectrum of the TiO₂ termination. The region close to the Fermi level (black line) was measured at a closer tip-sample distance than the rest of the spectrum (gray). (d) Unit cell grid superimposed on the atomically resolved AFM image.

$\eta(\text{Vac}) = (14 \pm 2)\%$. This concentration was constant and reproducible in all experiments.

Complementary to the vacancies on the SrO termination, the TiO_2-terminated surface is covered with point defects in the form of adatoms, seen in Fig. 3(b). These adatoms are imaged as depressions in the constant-height AFM image, reflecting an attractive chemical force with the tip. The underlying TiO_2 lattice is not resolved due to the dominant contribution of the geometrically protruding adatoms. The constant-height STM image [Fig. 3(a)], obtained simultaneously with the atomically resolved AFM image [Fig. 3(b)], shows that the current signal stems almost exclusively from the adatoms. The brightest species in the STM image [Fig. 3(a)] are probably linked to extrinsic impurities (Nb dopants). The brightness of the spots shows some variance in both the STM and AFM images (see Fig. S4 for details). The concentration of the adatoms $\eta(\text{Ad}) = (14 \pm 2)\%$ equals the vacancy concentration on the SrO-terminated surface areas, and the adatoms also sit in equivalent lattice positions [see Fig. 3(d)].

The electronic properties of the two surface terminations are dramatically different, as revealed by STS data in Figs. 2(c) and 3(c). The SrO termination appears as a wide-gap semiconductor, with the conduction band minimum located almost 2 eV above the Fermi level. On the other hand, the TiO_2 termination is metallic; the Fermi level crosses the bottom of the conduction band and a small density of states is detected throughout the whole band gap.

Based on their electronic fingerprints, the same concentration, and their specific lattice sites, we attribute the point defects present on both terminations as strontium vacancies on the SrO termination and complementary strontium adatoms on the TiO_2 termination. Sr adatoms act as electron donors and are responsible for the metallic nature of the TiO_2 termination. The ionized Sr^{2+} adatoms tend to be distributed across the surface to reduce electrostatic repulsion. Strontium vacancies act as negatively charged acceptor impurities and are responsible for the upward shift of the SrO conduction band. The locally measured STS spectra above the Sr vacancies exhibit an upward shift of 0.2 V compared to the defect-free regions [the green curve in Fig. 2(c)]. This defect-induced band bending is responsible for the empty-state STM image contrast in Fig. 2(a): The defects appear as dark depressions (marked by the green circles) due to the upwards band shift. Kelvin probe spectroscopy measurements above the Sr vacancies consistently show a band shift in the same direction, but weaker compared to the STS measurements (see Fig. S5). We note that the only other possible intrinsic point defects, O vacancies on SrO, and O adatoms on TiO_2 planes, would lead to electronic effects opposite to what is observed experimentally.

The large-area morphology of the as-cleaved surface, shown in Figs. 4(a)–4(c), provides valuable insight into the fracturing mechanism behind successful cleavage. The typical domain size of the SrO/TiO_2 terminations is much larger than the maximum scan range of our STM/AFM (>1 μm). Interestingly, steps do not switch the termination type and are mostly one unit cell high ($\approx$0.4 nm), or an integer multiple of that. Figure 4(a) shows a staircase of atomically flat terraces with TiO_2 termination, separated by unit-cell-high steps. Figure 4(b) shows an area with a more complex morphology containing multisteps; all the terraces here have the SrO
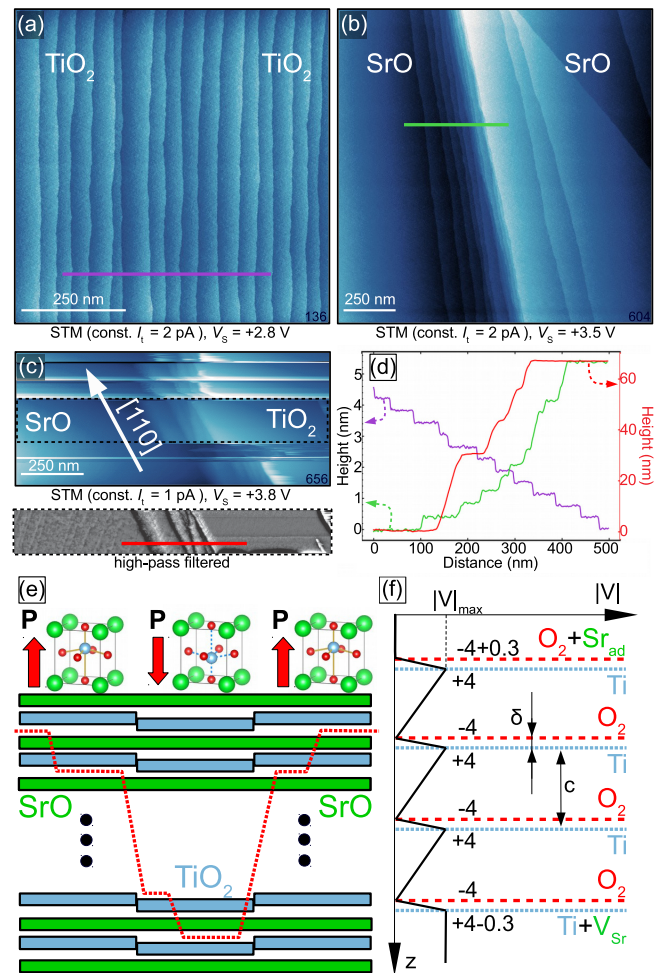

FIG. 4. Spatial distribution of surface terminations and a proposed model for ferroelectricity-assisted cleavage. (a) TiO_2 termination with a series of unit-cell-high steps. (b) SrO termination with a steep 6-nm staircase. (c) Change in termination associated with a $\approx$60 nm high step. The region between the broken lines is displayed below after high-pass filtering. (d) Line profiles measured along the blue, green, and red lines in (a)–(c), respectively. (e) Proposed scheme of the induced polarized domains and the fracturing mechanism. The red, dotted line shows the distribution of surface terminations with respect to the polarization orientation. (f) Electrostatic potential in a ferroelectric, polar, STO crystal with polarization compensation in the form of Sr adatoms and vacancies on opposing surfaces.

termination. The surface termination switches exclusively at very high steps, on the order of 100 nm, which are oriented in the [110] direction (parallel to the applied strain). This is illustrated in Fig. 4(c), where a multistep $\approx$60 nm high separates the SrO termination (left) from the TiO_2 termination (right).

The observed distribution of the SrO and TiO_2 terminations indicates that large bulk domains might be involved in the cleavage process. We propose a mechanism based on strain-induced ferroelectricity, illustrated in Fig. 4(e). The main feature of the ferroelectric phase in perovskites is an either positive or negative displacement of the B-site transition-metal atom along the [001] direction [27]. The displacement direction is coherent within a ferroelectric domain and results

in a spontaneous electric polarization **P** along the [001] direction [see the top row of Fig. 4(e)]. In a simple electrostatic picture, this distortion separates the formally electroneutral TiO_2 layers into two layers with formally equal and opposite charges, Ti^{4+} and $(O_2)^{4-}$. The distorted TiO_6 octahedra create inequivalent (001) planes suitable for cleaving [bottom scheme in Fig. 4(e)], where the resulting surface termination (SrO/TiO_2) does not change within the whole ferroelectric domain. The surface termination can only switch at ferroelectric domain walls, which, at the surface, are associated with very large steps. The observed domain size is in the range of few μm, and the orientation of the steps is consistent with observations made on various thin films grown on $SrTiO_3$, where the domain walls run along the main crystallographic directions [32–34].

Our cleaving device is designed to induce the ferroelectric phase transition by a combination of compressive strain from the sample mount, and tensile strain induced by external cleaving force. $SrTiO_3$ requires biaxial compressive strain of 1% to become ferroelectric at room temperature [26], or even higher uniaxial compressive strain. In our setup used for *in situ* cleaving, the maximum achievable strain is estimated as <0.4% (see Fig. S6). This is clearly below the value necessary for the ferroelectric phase transition, but it already guarantees a good cleavage. The main role in the ferroelectric phase transition is therefore played by the tensile strain present at the tip of the crack, which propagates through the crystal during the cleavage [35]. The compressive strain from the sample mount serves mainly to confine the tensile strain into a well-defined region, and allows tuning the size of the ferroelectric domains. This is demonstrated in Fig. S7 on a different perovskite, $KTaO_3$.

An important observation is the formation of Sr adatoms and vacancies in a well-defined concentration of $\eta(Sr_{Ad}) = \eta(V_{Sr}) = (14 \pm 2)\%$ in all our successful cleaving experiments. This indicates that they are intrinsic to surface stability. The ideal STO bulk crystal consists of alternating, weakly polar SrO and TiO_2 layers, which would not cause a polar catastrophe when cleaved, since the bond breaking and an increase of bond covalency at the surface layer would serve as a sufficient polarity compensation mechanism [36]. However, the cleavage occurs while the crystal is ferroelectric, and here the separation of Ti^{4+} and $(O_2)^{4-}$ layers renders the resulting surfaces polar. The removal of Sr^{2+} from the SrO and their addition to the TiO_2 termination therefore seems to serve as a mechanism for compensating the ferroelectricity-induced surface polarity [37].

A simplified model is sketched in Fig. 4(f). The ferroelectric, polar STO crystal is represented as stacking of three inequivalent layers along the [001] direction: A negatively charged $(O_2)^{4-}$ layer, a positively charged Ti^{4+} layer, and a formally electroneutral SrO layer, which we neglect in the electrostatic considerations. The Sr^{2+} adatoms and V_{Sr}^{2-} vacancies are represented by a surface layer with a formal charge density $\sigma = \pm 2 \times (0.14 \pm 0.2) \approx \pm 0.3$ electrons per unit cell. The electrostatic potential resulting from the polarization will cancel out with the additional potential from the surface defects: $|V| = \frac{4\delta}{\epsilon A} = \frac{\sigma c}{2\epsilon}$. Here V is the drop of electrostatic potential on one unit cell distance, δ is the separation of the Ti and O_2 layers due to the applied strain, ϵ is the dielectric permittivity, and c is the lattice constant, and A is the unit-cell area. This relation gives an estimate for the distortion δ as 3.7% c, which seems reasonable. The formation of charged surface defects therefore points to an interesting interplay between ferroelectricity and surface polarity. Since the cleavage occurs when the crystal is in its ferroelectric state, it is likely that the polarization remains in the near-surface region after the cleavage, stabilized by the charge of the surface defects. The observed defect concentration is independent of the compressive strain applied by our cleaving device. This is consistent with the assumption that the dominant factor in the ferroelectric phase transition is the high tensile strain at the tip of the crack: The magnitude of this strain is always identical, and corresponds to the tensile strength of $SrTiO_3$.

In summary, we have prepared bulk-terminated (001) surfaces of $SrTiO_3$, acquired atomically resolved images, and characterized the surface electronic structure and intrinsic defects of the resulting TiO_2 and SrO planes. This was made possible by using a simple cleavage device that prestrains the sample in a well-defined way: strain-induced ferroelectricity during cleaving breaks the cubic symmetry. As shown on $KTaO_3$, our cleaving method is applicable to other perovskites that exhibit (incipient) ferroelectricity. As it results in μm domains of single terminations, it opens up the opportunity to probe fundamental surface properties of cubic perovskites and heterostructures. Moreover, our work provides a showcase for how the surface stability of (incipient) ferroelectric materials is determined by balance between surface polarity, ferroelectric lattice polarization, and charged point defects.

---

[1] M. A. Pena and J. L. G. Fierro, Chemical structures and performance of perovskite oxides, Chem. Rev. **101**, 1981 (2001).

[2] J. B. Goodenough, Electronic and ionic transport properties and other physical aspects of perovskites, Rep. Prog. Phys. **67**, 1915 (2004).

[3] A. Ohtomo and H. Hwang, A high-mobility electron gas at the $LaAlO_3/SrTiO_3$ heterointerface, Nature (London) **427**, 423 (2004).

[4] K. Domen, A. Kudo, and T. Onishi, Mechanism of photocatalytic decomposition of water into H_2 and O_2 over $NiO-SrTiO_3$, J. Catal. **102**, 92 (1986).

[5] D. G. Schlom and J. Mannhart, Oxide electronics: Interface takes charge over Si, Nat. Mater. **10**, 168 (2011).

[6] S. Chambers *et al.*, Epitaxial growth and properties of ferromagnetic co-doped TiO_2 anatase, Appl. Phys. Lett. **79**, 3467 (2001).

[7] M. Kawasaki *et al.*, Atomic control of the SrTiO$_3$ crystal surface, Science **266**, 1540 (1994).

[8] W. Qing-Yan *et al.*, Interface-induced high-temperature superconductivity in single unit-cell FeSe films on SrTiO$_3$, Chin. Phys. Lett. **29**, 037402 (2012).

[9] A. Santander-Syro *et al.*, Two-dimensional electron gas with universal subbands at the surface of SrTiO$_3$, Nature (London) **469**, 189 (2011).

[10] Z. Wang *et al.*, Anisotropic two-dimensional electron gas at SrTiO$_3$ (110), Proc. Natl. Acad. Sci. USA **111**, 3933 (2014).

[11] W. Meevasana *et al.*, Creation and control of a two-dimensional electron liquid at the bare SrTiO$_3$ surface, Nat. Mater. **10**, 114 (2011).

[12] R. Herger, P. R. Willmott, O. Bunk, C. M. Schleputz, B. D. Patterson, B. Delley, V. L. Shneerson, P. F. Lyman, and D. K. Saldin, Surface structure of SrTiO$_3$(001), Phys. Rev. B **76**, 195435 (2007).

[13] S. A. Chambers, T. C. Droubay, C. Capan, and G. Sun, Unintentional F doping of SrTiO$_3$ (001) etched in HF acid-structure and electronic properties, Surf. Sci. **606**, 554 (2012).

[14] N. P. Guisinger *et al.*, Nanometer-scale striped surface terminations on fractured SrTiO$_3$ surfaces, ACS Nano **3**, 4132 (2009).

[15] W. Sitaputra, M. Skowronski, and R. M. Feenstra, Topographic and electronic structure of cleaved SrTiO$_3$ (001) surfaces, J. Vac. Sci. Technol. A **33**, 031402 (2015).

[16] T. Chien, T. S. Santos, M. Bode, N. P. Guisinger, and J. W. Freeland, Controllable local modification of fractured Nb-doped SrTiO$_3$ surfaces, Appl. Phys. Lett. **95**, 163107 (2009).

[17] See Supplemental Material at http://link.aps.org/supplemental/10.1103/PhysRevMaterials.3.034407 for additional experimental data.

[18] Q. Jiang and J. Zegenhagen, c (6 × 2) and c (4 × 2) reconstruction of SrTiO$_3$ (001), Surf. Sci. **425**, 343 (1999).

[19] S. Gerhold, Z. Wang, M. Schmid, and U. Diebold, Stoichiometry-driven switching between surface reconstructions on SrTiO$_3$ (001), Surf. Sci. **621**, L1 (2014).

[20] T. Kubo and H. Nozoye, Surface structure of SrTiO$_3$(100), Surf. Sci. **542**, 177 (2003).

[21] Z. Majzik *et al.*, Simultaneous current, force and dissipation measurements on the Si (111) 7 × 7 surface with an optimized qPlus AFM/STM technique, Beilstein J. Nanotechnol. **3**, 249 (2012).

[22] F. Huber and F. J. Giessibl, Low noise current preamplifier for qPlus sensor deflection signal detection in atomic force microscopy at room and low temperatures, Rev. Sci. Instrum. **88**, 073702 (2017).

[23] M. Setvin *et al.*, Ultrasharp tungsten tips-characterization and nondestructive cleaning, Ultramicroscopy **113**, 152 (2012).

[24] M. Prietsch, A. Samsavar, and R. Luedke, Structural and electronic properties of the Bi/GaP(110) interface, Phys. Rev. B **43**, 11850 (1991).

[25] M. Setvin *et al.*, Polarity compensation mechanisms on the perovskite surface KTaO$_3$ (001), Science **359**, 572 (2018).

[26] J. Haeni *et al.*, Room-temperature ferroelectricity in strained SrTiO$_3$, Nature (London) **430**, 758 (2004).

[27] W. Zhong and D. Vanderbilt, Competing Structural Instabilities in Cubic Perovskites, Phys. Rev. Lett. **74**, 2587 (1995).

[28] F. W. Lytle, X-ray diffractometry of low-temperature phase transformations in strontium titanate, J. Appl. Phys. **35**, 2212 (1964).

[29] U. Aschauer and N. A. Spaldin, Competition and cooperation between antiferrodistortive and ferroelectric instabilities in the model perovskite SrTiO$_3$, J. Phys.: Condens. Matter **26**, 122203 (2014).

[30] R. Bechstein *et al.*, 'All-inclusive' imaging of the rutile TiO$_2$(110) surface using nc-AFM, Nanotechnology **20**, 505703 (2009).

[31] A. S. Foster, C. Barth, and C. R. Henry, Chemical Identification of Ions in Doped NaCl by Scanning Force Microscopy, Phys. Rev. Lett. **102**, 256103 (2009).

[32] Y. Frenkel *et al.*, Imaging and tuning polarity at SrTiO$_3$ domain walls, Nat. Mater. **16**, 1203 (2017).

[33] B. Kalisky *et al.*, Locally enhanced conductivity due to the tetragonal domain structure in LaAlO$_3$/SrTiO$_3$ heterointerfaces, Nat. Mater. **12**, 1091 (2013).

[34] P. Zubko, N. Stucki, C. Lichtensteiger, and J.-M. Triscone, X-Ray Diffraction Studies of 180° Ferroelectric Domains in PbTiO$_3$/SrTiO$_3$ Superlattices Under an Applied Electric Field, Phys. Rev. Lett. **104**, 187601 (2010).

[35] A. A. Griffith, The phenomena of rupture and flow in solids, Philos. Trans. R. Soc. London A **221**, 163 (1921).

[36] J. Goniakowski, F. Finocchi, and C. Noguera, Polarity of oxide surfaces and nanostructures, Rep. Prog. Phys. **71**, 016501 (2007).

[37] C. Noguera, Polar oxide surfaces, J. Phys.: Condens. Matter **12**, R367 (2000).